



# High-Speed 1030 nm Anti-Waveguide VCSELs With 25 GHz Modulation Bandwidth

Yanjing Wang , Haixia Tong, Cunzhu Tong , Senior Member, IEEE, Bo Meng, Sicong Tian, Member, IEEE, Lijie Wang, and Lijun Wang

**Abstract**—We present the design, fabrication, and performance of high-speed oxide-confined 1030 nm vertical-cavity surface-emitting lasers (VCSELs) with a short anti-waveguiding optical cavity. By using a half-wavelength cavity to enhance the limit of the optical field, the anti-waveguide design increases the oscillator strength, thus promoting high-speed modulation. We carefully optimized the multiple quantum wells and the doping profile in order to achieve high-speed operation. The developed VCSELs exhibit a modulation bandwidth exceeding 25.1 GHz at 25 °C, supporting back-to-back data rates up to 40 Gb/s under binary non-return-to-zero (NRZ) modulation.

**Index Terms**—Vertical-cavity surface-emitting laser, high-speed, modulation bandwidth.

## I. INTRODUCTION

THE short-reach optical links based on 850 nm GaAs-based VCSELs over up to 100 m multimode fibers (MMF) have been widely deployed in large scale data centers [1], [2], [3]. However, the high chromatic dispersion of fiber and attenuation at this wavelength are important factors limiting transmission distance [4], [5]. At 850 nm, the fiber chromatic dispersion is as high as  $\sim 85$  ps/nm/km and the attenuation exceeds 2 dB/km [6], [7]. With data centers growing in size, the increased demand for longer reach optical interconnects (up to 2 km in large scale data centers [5]) drives the development of longer wavelength VCSELs so that the reach limitations of the 850 nm multimode links can be overcome.

Manuscript received 18 February 2023; revised 17 March 2023; accepted 20 March 2023. Date of publication 23 March 2023; date of current version 5 April 2023. This work was supported in part by the National Key Research and Development Program of China under Grants 2018YFB2201000 and 2021YFB2801000, in part by the National Natural Science Foundation of China under Grants 62121005 and 62174159, in part by the Open Fund of State Key Laboratory of High Power Semiconductor Lasers under Grant 2022-CCLG-ZDSYS-005, and in part by K. C. Wong Talent Program of Chinese Academy of Sciences. (Corresponding author: Cunzhu Tong.)

Yanjing Wang, Bo Meng, Sicong Tian, and Lijun Wang are with the State Key Laboratory of Luminescence and Application, Changchun Institute of Optics, Fine Mechanics and Physics, Chinese Academy of Sciences, Changchun 130033, China (e-mail: wangyanjing@ciomp.ac.cn; mengbo@ciomp.ac.cn; tiansicong@ciomp.ac.cn; wanglj@ciomp.ac.cn).

Cunzhu Tong and Lijie Wang are with the State Key Laboratory of Luminescence and Application, Changchun Institute of Optics, Fine Mechanics and Physics, Chinese Academy of Sciences, Changchun 130033, China, and also with the Jlight Semiconductor Technology Co., Ltd, Changchun 130033, China (e-mail: tongcz@ciomp.ac.cn; wanglijie@ciomp.ac.cn).

Haixia Tong is with the State Key Laboratory of High Power Semiconductor Lasers, School of Physics, Changchun University of Science and Technology, Changchun 130022, China (e-mail: tonghaixia18@mails.ucas.ac.cn).

Digital Object Identifier 10.1109/JPHOT.2023.3260924

The ideal wavelength is 1310 nm where chromatic dispersion is near zero and the attenuation of MMF is only  $\sim 0.4$  dB/km [6], [7]. Up to now, 1310 nm VCSELs have been developed based on quantum-dot [8] and InP material [9], [10]. However, the GaAs-based VCSEL technology, which is superior to the InP-based in terms of speed, efficiency, manufacturability and cost-efficiency, can only be extended to  $\sim 1100$  nm using conventional compound semiconductors without compromising reliability [11]. This has created an interest in GaAs-based VCSELs at wavelengths just below 1100 nm where the fiber chromatic dispersion is  $\sim 30$  ps/nm/km and the attenuation is below 1 dB/km [6], [7], a large improvement with respect to 850 nm.

For the purpose of extending the wavelength without compromised reliability [11], [12], GaAs-based VCSEL with wavelength  $\sim 1100$  nm was developed. Using the strained InGaAs/GaAs quantum wells (QWs) with doped barriers for high differential gain and reduced gain compression, oxide-confined VCSELs at 1090 nm with a modulation bandwidth of 20 GHz were demonstrated in 2006 [13]. Then a bottom-emitting VCSEL with a bandwidth of 18 GHz using multiple oxide apertures for low capacitance were demonstrated [14]. Furukawa demonstrated 20 GHz bandwidth oxide confined 1060 nm VCSELs using double intra-cavity structure and a dielectric top distributed Bragg reflector (DBR) [15], [16], [17], [18]. Recently, 1060 nm VCSELs utilizing strained InGaAs/GaAsP QWs and multiple oxide apertures with a bandwidth of 22 GHz were realized with similar techniques of commercial VCSELs [19], [20], [21].

An effective way to improve the performance of VCSEL devices is to apply an anti-waveguiding design [22], where the cavity region has a smaller refractive index compared to the average refractive index of a DBR. The anti-waveguiding VCSEL design aimed to suppress the highly undesirable in-plane fundamental mode, which is very important to avoid gain depletion and enhance the oscillator strength for the vertical transition. In this article, we demonstrate the use of an anti-waveguide structure design in the 1030 nm VCSEL. The optimized anti-waveguide structure exhibits better in plane mode suppression effects than traditional anti-waveguide structures. The modulation bandwidth of the VCSEL is 25.1 GHz and the data transmission at rates up to 40 Gb/s is demonstrated at 25 °C. The design and fabrication of the VCSEL are presented in Section II and their static characteristics are presented in Section III. Section IV is devoted to small-signal modulation. Section V is devoted to the large-signal modulation and a conclusion is presented in Section VI.

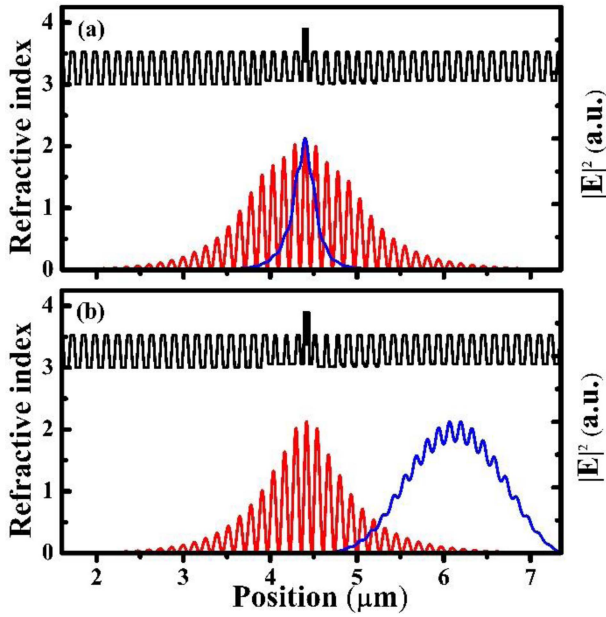


Fig. 1. Profiles of the refractive index and of the optical field strength of the VCSEL mode: (a) Conventional anti-waveguide  $\lambda/2$ -cavity design; (b) our  $\lambda/2$ -cavity design. Black: Refractive index profile, red: Vertical profile of the longitudinal VCSEL mode, blue: Vertical profile of the in-plane waveguiding mode.

## II. VCSEL DESIGN AND FABRICATION

The 1030 nm VCSEL epitaxy material was grown by metalorganic chemical vapor deposition. The first 26 pairs bottom DBR are made of AlAs/GaAs to reduce the thermal impedance. All other mirrors are made of  $\text{Al}_{0.9}\text{Ga}_{0.1}\text{As}/\text{GaAs}$ . The DBRs are with graded interfaces and modulation doping for the low resistance and internal optical loss. Multiple oxide apertures are placed in the p-DBR just above the active region. For high longitudinal optical confinement, we use a half-wavelength ( $\lambda/2$ ) thick cavity. The active region is positioned in a thin separate confinement heterostructure at the center of  $\lambda/2$  cavity. We have adopted the anti-waveguide design. Compared with the average refractive index of DBR, the refractive index of the cavity area is lower. The design of VCSELs with anti-waveguide cavities is an effective way to achieve high modulation bandwidth, which is broadly used by the industry [23]. Fig. 1(a) shows the vertical profiles of the refractive index, of the vertical cavity mode (red), and of the in-plane mode (blue) for a conventional anti-waveguide  $\lambda/2$ -cavity device. The in-plane mode electric field intensity in the active region is approximately the same as the vertical cavity mode. This will lead to the parasitism of in-plane laser, thus reducing the intensity of vertical oscillation. Fig. 1(b) shows our design of a  $\lambda/2$ -cavity device. The structures in both top/bottom DBRs and the  $\lambda/2$  cavity were carefully designed to shift the fundamental in-plane mode from the cavity region into the DBR. The electric field strength ( $|E|$ ) of the in-plane mode in the active region is about 9 times lower than that of the vertical mode. Furthermore, the in-plane mode has significant losses due to leakage into the top DBR, and the oscillator strength of the vertical mode is enhanced compared to the conventional anti-waveguide

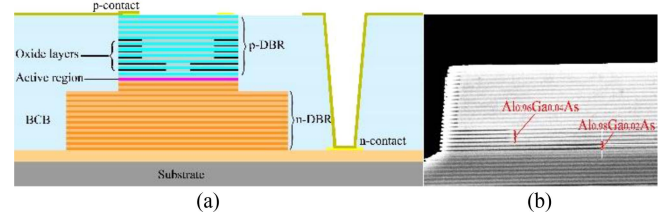


Fig. 2. (a) Schematic cross-section of the VCSEL structure. (b) SEM image of the cross section of the device, the dark lines are the oxidized high Al-composition layers in the p-DBR stack.

$\lambda/2$ -cavity VCSEL, which supports a high modulation bandwidth.

In the active region, we use partially strain-compensated InGaAs/GaAsP QWs, with net compressive strain. Above the active region is a p-DBR stack with 2 pairs of  $\text{Al}_{0.98}\text{Ga}_{0.02}\text{As}/\text{GaAs}$ , 4 pairs of  $\text{Al}_{0.96}\text{Ga}_{0.04}\text{As}/\text{GaAs}$ , 14 pairs of  $\text{Al}_{0.9}\text{Ga}_{0.1}\text{As}/\text{GaAs}$  and finally a GaAs contact layer. Transverse optical and current confinement is mainly provided by two  $\text{Al}_{0.98}\text{Ga}_{0.02}\text{As}$  layers after wet oxidation. The four  $\text{Al}_{0.96}\text{Ga}_{0.04}\text{As}$  layers are used to reduce the parasitic capacitance of oxide apertures.

The fabrication process starts with a 22- $\mu\text{m}$  diameter DBR mesa defined by inductively coupled plasma dry etching. A laser interferometry apparatus was used to monitor the etching. Right after the dry etching, the sample was sent to an oxidation furnace filled with  $\text{H}_2\text{O}$  vapor and  $\text{N}_2$  carrier gas to laterally oxidize the high Al-composition layers in the top p-DBR, the aperture and parasitic reduction oxide layers. Side view scanning electron microscopy (SEM) images of the oxide layers are shown in Fig. 2(b). The p-type Ti/Pt/Au and n-type Ni/AuGe/Ni/Au metal contact was evaporated and annealed, respectively. The device fabrication is finished with benzocyclobutene planarization, via-hole etching, and Ti/Au metal interconnect evaporation. Schematic cross-section of the VCSEL structure is shown in Fig. 2(a).

## III. STATIC CHARACTERISTICS

The measured light-current-voltage (L-I-V) characteristics of the VCSELs with oxide-aperture diameters of  $\sim 5 \mu\text{m}$  at different temperature are shown in Fig. 3. From the L-I-V measurements, we extract the threshold currents depending on temperature. This data is presented in Fig. 4. The threshold current increases from  $I_{\text{th}} = 0.53 \text{ mA}$  at 25 °C to 0.76 mA at 45 °C, to 1.05 mA at 65 °C, and finally to 1.48 mA at 85 °C. At higher temperatures, the threshold current increases due to the increased optical absorption, reduced internal efficiency, and an increase of the gain-wavelength detuning (lower gain), and is close to twice the 25 °C value at 85 °C. The minimum threshold current for this device is below 25 °C.

Fig. 5 shows the lasing spectra of the device under the bias of  $I = 1.5 \text{ mA}$  (25 °C) and  $I = 4.5 \text{ mA}$  (85 °C). The bias current is about  $3I_{\text{th}}$ . A redshift of 5.38 nm was observed when the bias and temperature condition change. The root mean square (RMS) spectral width is 0.68 nm and 0.46 nm under 25 °C and 85 °C, respectively.

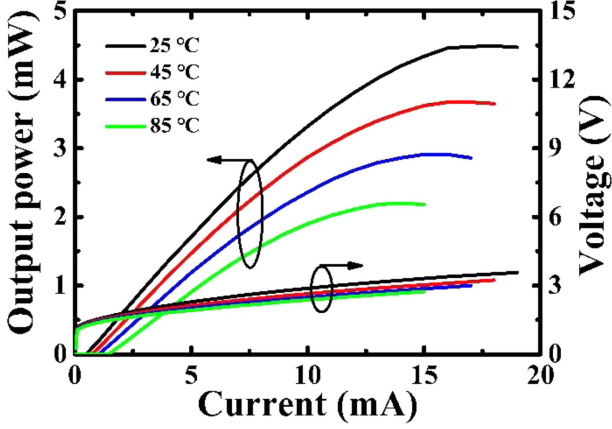


Fig. 3. L-I-V characteristics of the 1030 nm oxide-confined VCSEL from 25 °C to 85 °C.

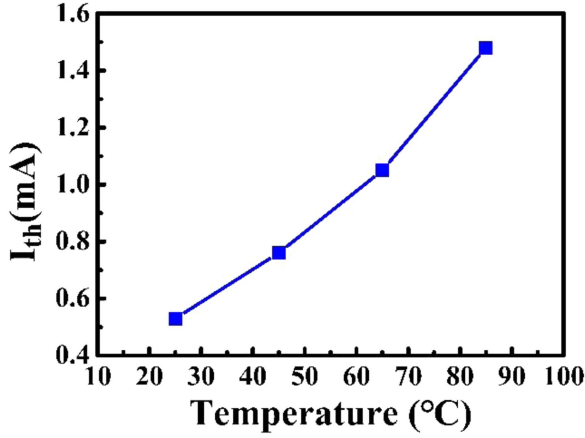


Fig. 4. Measured and fitting results of temperature dependent threshold current for the VCSEL.

#### IV. SMALL-SIGNAL MODULATION

The small-signal modulation response ( $S_{21}$ ) can be modelled as a second order damped system described by a resonance frequency  $f_r$  and a damping rate  $\gamma$  [24]. Accounting for both the intrinsic response of the laser and the extrinsic, parasitic response, giving the full three-pole transfer function

$$H(f) = A \cdot \frac{1}{1 + j(f/f_p)} \cdot \frac{f_r^2}{f_r^2 - f^2 + \gamma \cdot f / 2\pi}, \quad (1)$$

where  $A$  is an amplitude factor,  $f$  is the modulation frequency,  $f_p$  is the parasitic cut-off frequency. The parasitic transfer function may also be determined by  $S_{11}$  measurements, which also allow fitting values of the parasitic elements to an equivalent circuit model [25].

The resonance frequency increases linearly with the square root of bias current above threshold according to

$$f_r = D \sqrt{I - I_{th}}. \quad (2)$$

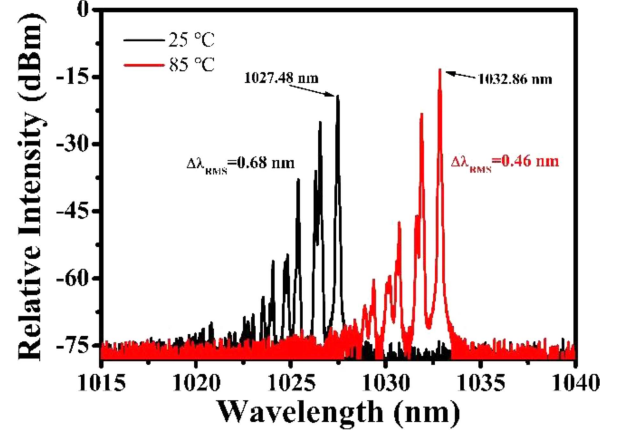


Fig. 5. The optical spectrum of the VCSEL at two biasing and temperature conditions: The black curve represents room temperature measurement at  $I = 1.5$  mA ( $I/I_{th} \approx 3$ ) and the red curve represents 85 °C measurement at  $I = 4.5$  mA ( $I/I_{th} \approx 3$ ).

With

$$D = \frac{1}{2\pi} \cdot \sqrt{\frac{\eta_i \Gamma \nu_g}{q L_a} \frac{\partial g / \partial n}{\chi}}, \quad (3)$$

where  $\eta_i$  is the internal quantum efficiency,  $\Gamma$  is the optical confinement factor,  $\nu_g$  the group velocity,  $L_a$  the total thickness of the QWs,  $\partial g / \partial n$  is the differential gain, and  $\chi$  the transport factor. VCSELS with a large D-factor and low threshold current reach high resonance frequencies at low bias currents, which enables energy-efficient high-speed modulation. A large D-factor is also important in order to reach a high maximal VCSEL bandwidth, equivalent to reaching a large resonance frequency before current induced self-heating and thermal saturation deteriorates performance.

The damping is increasing linearly with the square of the resonance frequency and determines an intrinsic upper limit to the modulation bandwidth. The rate at which damping increases is quantified by the K-factor

$$\gamma = K \cdot f_r^2 + \gamma_0. \quad (4)$$

With

$$K = 4\pi^2 \left( \tau_p + \frac{\varepsilon \chi}{\nu_g \partial g / \partial n} \right), \quad (5)$$

where  $\varepsilon$  is the gain compression factor,  $\tau_p$  is the photon lifetime and the offset  $\gamma_0$  is approximately equal to the inverse differential carrier lifetime [24].

The small signal modulation response was measured using a 67 GHz vector network analyzer (Keysight) connected to the VCSEL under test through a high-speed bias-T and a high-speed RF probe (Picoprobe). The VCSELS were probed directly on wafer and the light was coupled into an angled multimode fiber and then was fed to a 30 GHz photodetector (Thorlabs) via a variable optical attenuator (VOA) to avoid saturation of the detector. The measured data was corrected for the limited frequency response of the probe and detector.

Fig. 6(a) and (b) show the small signal modulation response ( $S_{21}$ ) at 25 °C and 85 °C, respectively, and plotted together



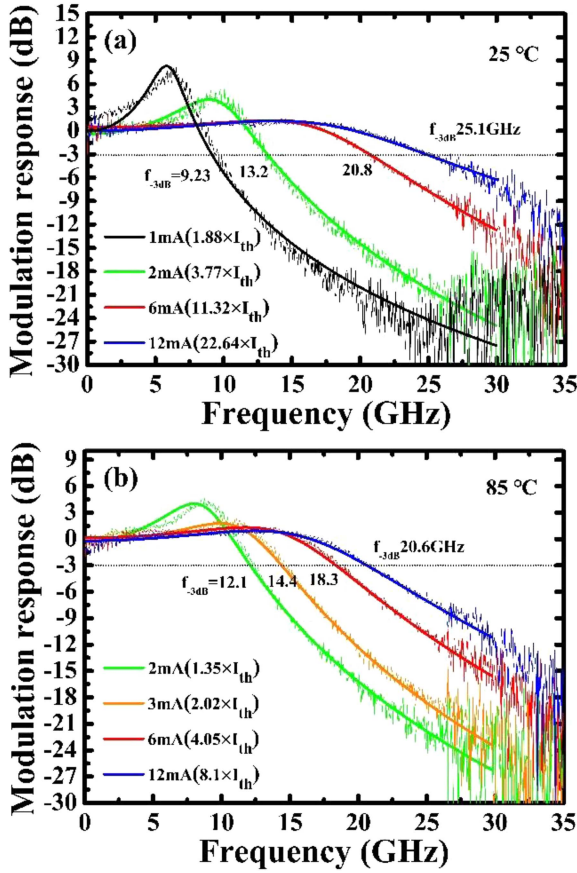


Fig. 6. Small signal modulation response for VCSEL (a) 25 °C and (b) 85 °C at indicated bias currents.

with fits to a three-pole transfer function (1). The low frequency roll-off which is most pronounced at low bias in Fig. 6(a) and (b) is attributed to excessive damping from spatial hole burning [26]. The 5  $\mu\text{m}$  aperture VCSEL reaches a maximum bandwidth of 25.1 GHz and 20.6 GHz at 12 mA under 25 °C and 85 °C, respectively. There are more significant 3dB drops in S21 at higher bias current, which can be attributed to the thermal rollover of  $f_r$  under high bias current.

A three-pole transfer function (1) was fitted to the measured data to extract the resonance frequency and the damping rate. By plotting of  $f_r$  against  $\sqrt{I - I_{th}}$ , the D-factor of the VCSEL can be extracted. Fig. 7 shows the  $f_r$  plotted against the square root of bias current ( $I$ ) above threshold ( $I_{th}$ ) under different temperature conditions. The extracted D-factor is 7.8 GHz/mA<sup>1/2</sup> and the  $f_r$  saturates at a maximum value of  $\sim 22$  GHz at 25 °C. Increasing the temperature to 85 °C only results in a minor reduction of the D-factor to 7.2 GHz/mA<sup>1/2</sup>, but since thermal saturation sets in earlier at this temperature, the maximum resonance frequency is reduced more noticeably to  $\sim 19$  GHz. The D-factor is relatively temperature stable, dropping only 14% from 25 to 85 °C. The D-factor is smaller for higher operating temperatures. The reason is that the internal quantum efficiency decreases with the increase of temperature. K-factors were extracted from linear fits of (4) as seen in Fig. 8. The K-factors were extracted from the low current regime, before thermal saturation begins, and were

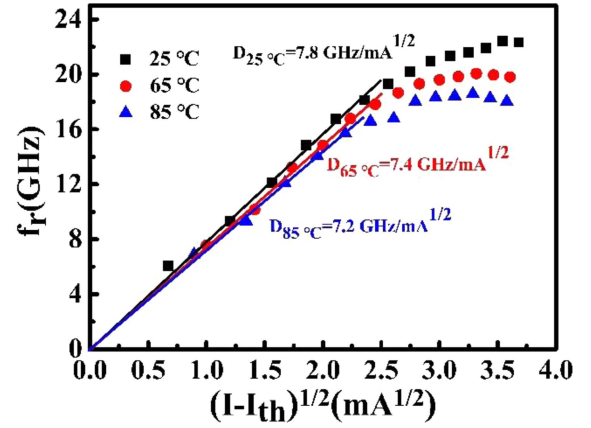


Fig. 7. Fitted resonance frequency,  $f_r$ , vs.  $\sqrt{I - I_{th}}$  plots at 25 °C, 65 °C, and 85 °C. The fitted slope of the data points in the linear region corresponds to the D-factor.

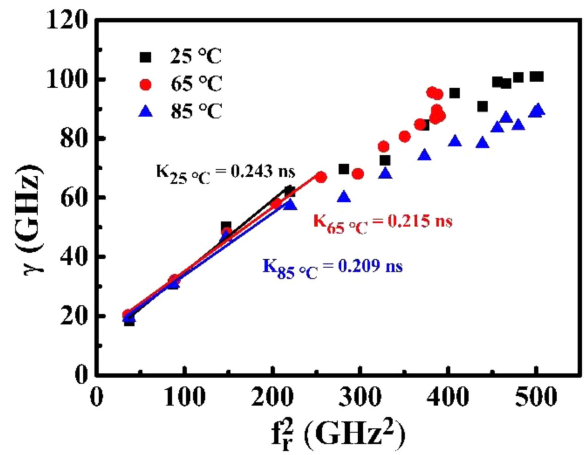


Fig. 8. Fitted damping rate,  $\gamma$ , vs. fitted resonance frequency squared,  $f_r^2$ , at 25 °C, 65 °C, and 85 °C.

found to be relatively temperature insensitive at 0.243–0.209 ns from 25 to 85 °C, showing a relatively weak temperature dependence. This can be explained by the differential gain change with temperature. The differential gain of the quantum well will increase slightly with the increase of temperature. It can be seen from (5) that the K factor decreases with the increase of differential gain.

## V. LARGE-SIGNAL MODULATION

To validate the device's data-transmitting capability, we perform the eye diagram and bit-error-rate (BER) measurement. The transmission interconnect setup consists of a SHF Bit Pattern Generator (BPG) that provides the modulation bit sequence, the same light collimation module used for DC and RF measurements, a 2 m and 100m OM5 optical fiber that collects the coupled light from the light collimation module, and a Thorlabs 30 GHz photoreceiver that converts the collected optical signal back into electrical signal. The test bit sequence used is a non-return-to-zero 2<sup>7</sup>-1 by the SHF BPG. The converted

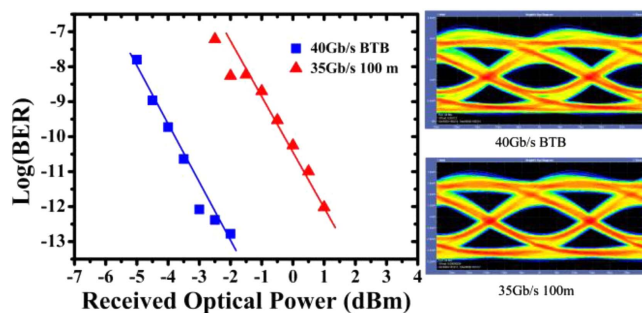


Fig. 9. Eye diagrams and BER measurement at 40 Gb/s BTB and at 35 Gb/s 100 m under the bias of  $I = 10$  mA and at 25 °C.

electrical signal from the photoreceiver is sent to the SHF Error Analyzer for BER testing. A Tektronix Oscilloscope with a 59 GHz bandwidth sampling module is used to capture the eye diagrams.

Fig. 9 shows the results of the back-to-back (BTB,  $\sim 2$  m OM5 MMF) and 100 m (OM5 MMF) transmission experiments at 25 °C. At  $I = 10$  mA, the VCSEL is able to demonstrate transmission at 40 Gb/s (BTB) and 35 Gb/s (100 m). The eyes are clearly open and BER  $< 10^{-12}$  is reached in both cases. The VCSEL also has a large RMS spectral width ( $> 0.6$  nm) and because of modal fiber dispersion, it is unable to achieve longer distance ( $> 100$  m) transmission.

## VI. CONCLUSION

In conclusion, we have demonstrated a high-speed 1030 nm VCSELS with a short optical cavity and multiple oxide apertures. The use of a short  $\lambda/2$  cavity improves the longitudinal confinement factor and the dynamic properties. To reduce capacitance, we use multiple oxide apertures with two primary apertures for transverse optical and current confinement and four secondary oxidizable AlGaAs layers for parasitic capacitance reduction. Applying an anti-waveguiding cavity leads to a strong suppression of parasitic in-plane optical modes, which supports a high modulation bandwidth. The 1030 nm VCSEL with  $\sim 5$   $\mu\text{m}$  aperture demonstrated a bandwidth of 25.1 GHz at 25 °C, and can be modulated for error-free data transmission at rates up to 40 Gb/s. Our device is promising to be used as high-speed transmitters in the next generation data centers.

## REFERENCES

- [1] J. A. Tatum et al., "VCSEL-based interconnects for current and future data centers," *J. Lightw. Technol.*, vol. 33, no. 4, pp. 727–732, Feb. 2015, doi: [10.1109/JLT.2014.2370633](https://doi.org/10.1109/JLT.2014.2370633).
- [2] D. Mahgerefteh et al., "Techno-economic comparison of silicon photonics and multimode VCSELS," *J. Lightw. Technol.*, vol. 34, no. 2, pp. 233–242, Jan. 2016, doi: [10.1109/JLT.2015.2483587](https://doi.org/10.1109/JLT.2015.2483587).
- [3] A. Tatarczak et al., "Reach extension and capacity enhancement of VCSEL-based transmission over single-lane MMF links," *J. Lightw. Technol.*, vol. 35, no. 4, pp. 565–571, Feb. 2017, doi: [10.1109/JLT.2016.2615815](https://doi.org/10.1109/JLT.2016.2615815).
- [4] M. J. Li, "MMF for high data rate and short length applications," in *Proc. Opt. Fiber Commun.*, 2014, pp. 1–3.
- [5] Y. Sun, "Recent advances for high speed short reach optical interconnects for datacom links," in *Proc. IEEE Compon., Packag., Manuf. Technol. Symp.*, 2017, pp. 63–65.
- [6] M. J. Li, "Novel optical fibers for data center applications," *Proc. SPIE*, vol. 9772, 2016, Art. no. 977205, doi: [10.1117/12.2217734](https://doi.org/10.1117/12.2217734).
- [7] S. R. Bickham et al., "Low cutoff G.657-compatible fiber for data center interconnects operating in the 1064 and 1310 nm windows," *Proc. SPIE*, vol. 11286, 2020, Art. no. 112860C, doi: [10.1117/12.2547869](https://doi.org/10.1117/12.2547869).
- [8] C. Z. Tong, D. W. Xu, S. F. Yoon, Y. Ding, and W. J. Fan, "Temperature characteristics of 1.3- $\mu\text{m}$  p-doped InAs–GaAs quantum-dot vertical-cavity surface-emitting lasers," *IEEE J. Sel. Topics Quantum Electron.*, vol. 15, no. 3, pp. 743–748, May/Jun. 2009, doi: [10.1109/JSTQE.2008.2010235](https://doi.org/10.1109/JSTQE.2008.2010235).
- [9] S. Spiga, M. Müller, and M.-C. Amann, "Energy-efficient high-speed InP-based 1.3  $\mu\text{m}$  short-cavity VCSELS," in *Proc. IEEE 15th Int. Conf. Transparent Opt. Netw.*, 2013, pp. 1–4, doi: [10.1109/ICTON.2013.6602683](https://doi.org/10.1109/ICTON.2013.6602683).
- [10] A. Malacarne et al., "Optical transmitter based on a 1.3- $\mu\text{m}$  VCSEL and a SiGe driver circuit for short-reach applications and beyond," *J. Lightw. Technol.*, vol. 36, no. 9, pp. 1527–1536, May 2018, doi: [10.1109/JLT.2017.2782882](https://doi.org/10.1109/JLT.2017.2782882).
- [11] H. Hatakeyama et al., "Highly reliable high-speed 1.1  $\mu\text{m}$  range VCSELS with InGaAs/GaAsP MQW," *IEEE J. Quantum Electron.*, vol. 46, no. 6, pp. 890–887, Jun. 2010, doi: [10.1109/JQE.2010.2040583](https://doi.org/10.1109/JQE.2010.2040583).
- [12] J. Guenter, B. Hawkins, R. Hawthorne, and G. Landry, "Reliability of VCSELS for  $> 25$  Gb/s," in *Proc. Opt. Fiber Commun.*, 2014, pp. 1–3, doi: [10.1364/OFC.2014.M3G.2](https://doi.org/10.1364/OFC.2014.M3G.2).
- [13] N. Suzuki, H. Hatakeyama, K. Fukatsu, T. Anan, K. Yashiki, and M. Tsuji, "25 Gbit/s operation of InGaAs-based VCSELS," *Electron. Lett.*, vol. 42, no. 17, pp. 975–976, Aug. 2006, doi: [10.1049/el:20061649](https://doi.org/10.1049/el:20061649).
- [14] Y. Zheng, C. H. Lin, A. V. Barve, and L. A. Coldren, "P-type  $\delta$ -doping of highly strained VCSELS for 25 Gbps operation," in *Proc. IEEE Photon. Conf.*, 2012, pp. 131–132, doi: [10.1109/IPCon.2012.6358524](https://doi.org/10.1109/IPCon.2012.6358524).
- [15] T. Suzuki, M. Funabashi, H. Shimizu, K. Nagashima, S. Kamiya, and A. Kasukawa, "1060 nm 28 Gbps VCSEL development at Furukawa," *Proc. SPIE*, vol. 9001, pp. 20–28, 2014, doi: [10.1117/12.2042857](https://doi.org/10.1117/12.2042857).
- [16] T. Kise, T. Suzuki, M. Funabashi, K. Nagashima, and H. Nasu, "Development of 1060 nm 25-Gb/s VCSEL and demonstration of 300m and 500m system reach using MMFs and link optimized for 1060 nm," in *Proc. Opt. Fiber Commun. Conf.*, 2015, pp. 1–3.
- [17] J. B. Heroux et al., "Energy-efficient 1060-nm optical link operating up to 28 Gb/s," *J. Lightw. Technol.*, vol. 33, no. 4, pp. 733–740, Feb. 2015, doi: [10.1109/JLT.2015.2393888](https://doi.org/10.1109/JLT.2015.2393888).
- [18] K. Nagashima, T. Kise, Y. Ishikawa, and H. Nasu, "A record 1-km MMF NRZ 25.78-Gb/s error-free link using a 1060-nm DIC VCSEL," *IEEE Photon. Technol. Lett.*, vol. 28, no. 4, pp. 418–420, Feb. 2016.
- [19] E. Simpanen et al., "1060 nm VCSEL for up to 40 Gbit/s data transmission," in *Proc. IEEE Int. Semicond. Laser Conf.*, 2016, pp. 1–2.
- [20] A. Larsson et al., "1060 nm VCSELS for long-reach optical interconnects," *Opt. Fiber Technol.*, vol. 44, pp. 36–42, Aug. 2018, doi: [10.1016/j.yofte.2018.01.001](https://doi.org/10.1016/j.yofte.2018.01.001).
- [21] E. Simpanen et al., "1060 nm single-mode VCSEL and single-mode fiber links for long-reach optical interconnects," *J. Lightw. Technol.*, vol. 37, no. 13, pp. 2963–2969, Jul. 2019, doi: [10.1109/JLT.2019.2908249](https://doi.org/10.1109/JLT.2019.2908249).
- [22] N. Ledentsov and V. Shchukin, "Optoelectronic device based on an anti-waveguiding cavity," U.S. Patent 7,339,965, Mar. 2008.
- [23] N. N. Ledentsov et al., "Anti-waveguiding vertical-cavity surface-emitting laser at 850 nm: From concept to advances in high-speed data transmission," *Opt. Exp.*, vol. 26, no. 1, pp. 445–453, 2018.
- [24] L. A. Coldren and S. W. Corzine, *Diode Lasers and Photonic Integrated Circuits*. Hoboken, NJ, USA: Wiley, 2014.
- [25] Y. Ou, J. S. Gustavsson, P. Westbergh, A. Haglund, A. Larsson, and A. Joel, "Impedance characteristics and parasitic speed limitations of high speed 850-nm VCSELS," *IEEE Photon. Technol. Lett.*, vol. 21, no. 24, pp. 1840–1842, Dec. 2009, doi: [10.1109/LPT.2009.2034618](https://doi.org/10.1109/LPT.2009.2034618).
- [26] Y. Liu, W. C. Ng, B. Klein, and K. Hess, "Effects of the spatial nonuniformity of optical transverse modes on the modulation response of vertical-cavity-surface-emitting lasers," *IEEE J. Quantum Electron.*, vol. 39, no. 1, pp. 99–108, Jan. 2003, doi: [10.1109/JQE.2002.806205](https://doi.org/10.1109/JQE.2002.806205).